A Weak Value Amplification Scheme Based on Single-Particle Multi-Levels

Wenbo Su(苏闻博)[1,2], Peng Wang(王鹏)[1,2], Chunwang Wu(吴春旺)[1,2],
Wei Wu(吴伟)[1,2,3], and Pingxing Chen(陈平形)[1,2,3*]

[1]College of Science, National University of Defense Technology, Changsha 410073, China

[2]Hunan Key Laboratory of Mechanism and Technology of Quantum Information, Changsha 410073,

[3]Hefei National Laboratory, Hefei 230088, China

September 4, 2026

Abstract

Weak measurements have many applications in the field of quantum information due to the peculiar properties of weak values. Quantum weak measurement can be performed by two particles or two degree of freedom of single particle. The former needs complex operations, the latter require the reconstruction of the motion state wavepacket, which consumes substantial quantum resources. This paper presents a novel weak measurement scheme that encodes multiple internal energy levels of a single particle into the measured system and the measuring pointer, while defining a finite-coupling postselected pointer ratio (FCPR). The FCPR obtained from this scheme enables both weak value amplification and rapid experimental results. To verify these advantages, we measured the FCPR using a trapped $^{40}Ca^{+}$ experimental setup and monitored fluctuations of the laser power within the experimental system. The results show that our scheme can detect weaker laser power fluctuations, thus providing higher precision for laser power locking.

Keywords: weak measurement, trapped ion, weak value amplification

PACS: 03.65.Ta, 42.50.Dv, 37.10.Ty, 03.67.Lx

1. Introduction

Quantum weak measurement is a technique [1–7] for extracuting quantum information through the weak coupling between a measured system and a measuring pointer [8]. Its primary advantage lies in the fact that the measured 'weak value' exceeds the eigenvalue spectrum of the measurement operator, which enables the amplification of minute signals. This characteristic endows weak measurements with unique value in addressing critical challenges in quantum science, enabling both fundamental investigations, such as direct observations of wave functions [9,10], and quantum metrology [2,11–13]. To date, high-fidelity weak measurements have been successfully implemented across various advanced platforms, including photon polarization [14–18], superconducting circuits [19–22], and trapped ion systems [23–25].

*Corresponding author. E-mail: pxchen@nudt.edu.cn

The weak measurement schemes based on the trapped ion show some interesting features. For a two-particle system, the two-qubit quantum entanglement scheme [26,27] can be employed to achieve a controllable coupling between the measured system and the measuring pointer. However, the two-ion scheme relies on high-precision individual ion addressing and high-fidelity two-qubit entanglement gates, which impose significant challenges for experimental manipulation. With in a single particle system, the internal state of the trapped ion is typically defined as the measured system, while the external motional state serves as the measuring pointer. However, measuring the motion state of the ion requires reconstructing its wave function in phase space [23,28]. This process consumes substantial quantum resources and measurement time. To address these challenges, we mapped the scheme onto multiple internal energy levels of a single ion by encoding both the measured system and the measuring pointer onto spin states within a single ion. By measuring the internal state of the ion using the electron shelving technique, its probability distribution can be obtained rapidly, thereby significantly reducing the time required for a single weak measurement. Employing the quantum circuit decomposition method, we decomposed the two-qubit entangled hamiltonian into a sequence of single-qubit multi-level rotation operations [29]. This approach significantly reduces the experimental complexity while offering the prospect of achieving higher operational fidelity.

In this paper, we first theoretically constructed a weak measurement operator model encoded by two-ion internal states, and through quantum circuit decomposition, transformed it into an experimentally feasible single-ion multi-level encoding manipulation sequence. Subsequently, we successfully demonstrated the feasibility of this scheme on a trapped $^{40}Ca^{+}$ ion platform. In the theoretical analysis, rather than treating the postselected pointer response as a conventional weak value, we define the finite-coupling postselected pointer ratio (FCPR), denoted $\langle\hat{\sigma}_x\rangle_{FCPR}$, which is related to the conventional weak value $\langle\hat{\sigma}_x\rangle_w$ by $\langle\hat{\sigma}_x\rangle_{FCPR} = -i\tan\frac{g}{2}\langle\hat{\sigma}_x\rangle_w$. This FCPR inherits the amplification behavior of the weak value while also capturing the full postselected pointer response of the single-particle encoding. To demonstrate the advantages of rapid readout and weak value amplification, we apply the scheme to real-time monitoring of laser-power fluctuations within the experimental system. The results show that the scheme significantly reduces the data-acquisition time while maintaining high measurement precision, providing a practical route toward fast weak measurements and high-sensitivity monitoring in future quantum information processing.

2. Theoretical model

This section describes a theoretical scheme for weak measurements based on single-particle multi-level systems. To begin with, we introduce the fundamental theory of the weak measurement. In the weak measurement, the Hamiltonian describing the coupling between the measured system and the measuring pointer can be expressed as

$$H_I = g\hat{A}\otimes\hat{p}, \tag{1}$$

where g is the coupling strength between measured system and measuring pointer, $\hat{A}$ is the observable of measured system, and $\hat{p}$ is the observable of measuring pointer. If the measured system initial state is selected to be $|\psi\rangle$ and the postselection state is $|\psi_f\rangle$, the displacement of the measuring pointer can be measured as

$g\left|\left\langle \hat{A}\right\rangle_w\right|$, where $\left\langle \hat{A}\right\rangle_w$ is weak value and is defined as

$$\left\langle \hat{A}\right\rangle_w = \frac{\langle\psi_f|\hat{A}|\psi\rangle}{\langle\psi_f|\psi\rangle}. \tag{2}$$

According to Eq. (1), if the measuring pointer is a spin qubit, a two-qubit entanglement gate [26,27] provides a suitable Hamiltonian for coupling measured system and measuring pointer; its evolution operator can be written as:

$$U = e^{-i\frac{g}{2}\hat{\sigma}_x\otimes\hat{\sigma}_x}, \tag{3}$$

where $\hat{\sigma}_x$ Pauli operator, g is the coupling strength between measured system and measuring pointer. When employing the two-qubit scheme, following the standard procedure of weak measurement, we need to perform post-selection on the measured system using single-qubit addressing techniques. However, whether it involves single-qubit addressing techniques or two-qubit entanglement operations, their experimental methods are technically complex. Therefore, we propose mapping the two-qubit scheme onto multi-level states, employing the quantum circuit model to decompose two-qubit operations into single-qubit operations. First, let's define the spin states: $|\uparrow\rangle = \begin{pmatrix}1\\0\end{pmatrix}$ and $|\downarrow\rangle = \begin{pmatrix}0\\1\end{pmatrix}$. Encoding the two qubit state into a single qubit multi-level state can be defined as:

$$|1\rangle = |\uparrow\rangle\otimes|\uparrow\rangle = \begin{pmatrix}1\\0\\0\\0\end{pmatrix}, |2\rangle \quad = |\uparrow\rangle\otimes|\downarrow\rangle = \begin{pmatrix}0\\1\\0\\0\end{pmatrix}, |3\rangle = |\downarrow\rangle\otimes|\uparrow\rangle = \begin{pmatrix}0\\0\\1\\0\end{pmatrix}, |4\rangle \quad = |\downarrow\rangle\otimes|\downarrow\rangle = \begin{pmatrix}0\\0\\0\\1\end{pmatrix}. \tag{4}$$

Both the measured system state $|\psi_s\rangle$ and the measuring pointer state $|\psi_p\rangle$ are initialized to $|\uparrow\rangle$, and then the initial state of the whole system is $|1\rangle$. Weak measurement experiment requires that the initial state of the measured system be prepared as an arbitrary superposition state. Independent operations R_y on the measured system can be decomposed as follows:

$$\begin{aligned}
R_y(\theta)\otimes I &= \begin{pmatrix}\cos\frac{\theta}{2} & -\sin\frac{\theta}{2}\\ \sin\frac{\theta}{2} & \cos\frac{\theta}{2}\end{pmatrix}\otimes\begin{pmatrix}1&0\\0&1\end{pmatrix}\\
&= \begin{pmatrix}\cos\frac{\theta}{2} & 0 & -\sin\frac{\theta}{2} & 0\\ 0 & \cos\frac{\theta}{2} & 0 & -\sin\frac{\theta}{2}\\ \sin\frac{\theta}{2} & 0 & \cos\frac{\theta}{2} & 0\\ 0 & \sin\frac{\theta}{2} & 0 & \cos\frac{\theta}{2}\end{pmatrix}\\
&= \begin{pmatrix}\cos\frac{\theta}{2} & 0 & -\sin\frac{\theta}{2} & 0\\ 0 & 1 & 0 & 0\\ \sin\frac{\theta}{2} & 0 & \cos\frac{\theta}{2} & 0\\ 0 & 0 & 0 & 1\end{pmatrix}\begin{pmatrix}1&0&0&0\\0&\cos\frac{\theta}{2}&0&-\sin\frac{\theta}{2}\\0&0&1&0\\0&\sin\frac{\theta}{2}&0&\cos\frac{\theta}{2}\end{pmatrix}\\
&= R_{y_{13}}(\theta)\,R_{y_{24}}(\theta).
\end{aligned} \tag{5}$$

where θ is the internal state rotation angle, R_y denotes the single-qubit rotation gate, and $R_{y_{24}}$ represents performing a $\hat{\sigma}_y$ rotation on space supported by energy level $|2\rangle$ to energy level $|4\rangle$ with rotation angle θ. Using

circuit decomposition, the evolution operator in Eq. (3) can be decomposed into single-qubit operations:

$$
\begin{aligned}
e^{-i\frac{g}{2}\hat{\sigma}_x\otimes\hat{\sigma}_x} &= \begin{pmatrix} \cos\frac{g}{2} & 0 & 0 & -i\sin\frac{g}{2} \\ 0 & \cos\frac{g}{2} & -i\sin\frac{g}{2} & 0 \\ 0 & -i\sin\frac{g}{2} & \cos\frac{g}{2} & 0 \\ -i\sin\frac{g}{2} & 0 & 0 & \cos\frac{g}{2} \end{pmatrix} \\
&= \begin{pmatrix} \cos\frac{g}{2} & 0 & 0 & -i\sin\frac{g}{2} \\ 0 & 1 & 0 & 0 \\ 0 & 0 & 1 & 0 \\ -i\sin\frac{g}{2} & 0 & 0 & \cos\frac{g}{2} \end{pmatrix} \begin{pmatrix} 1 & 0 & 0 & 0 \\ 0 & \cos\frac{g}{2} & -i\sin\frac{g}{2} & 0 \\ 0 & -i\sin\frac{g}{2} & \cos\frac{g}{2} & 0 \\ 0 & 0 & 0 & 1 \end{pmatrix} \\
&= R_{x_{14}}(g)\, R_{x_{23}}(g)\,.
\end{aligned}
\tag{6}
$$

Here, applying the initial state preparation operation from Eq. (5) and the interaction operation from Eq. (6) to the initial state $|\psi_s\rangle \otimes |\psi_p\rangle$:

$$
\begin{aligned}
& e^{-i\frac{g}{2}\hat{\sigma}_x\otimes\hat{\sigma}_x}(R_y\otimes I)(|\psi_s\rangle\otimes|\psi_p\rangle) \\
&= R_{x_{14}}(g)\, R_{x_{23}}(g)\, R_{y_{13}}(\theta)\, R_{y_{24}}(\theta)\,|1\rangle \\
&= \begin{pmatrix} \cos(\frac{g}{2})\cos(\frac{\theta}{2}) \\ -i\sin(\frac{g}{2})\sin(\frac{\theta}{2}) \\ \cos(\frac{g}{2})\sin(\frac{\theta}{2}) \\ -i\sin(\frac{g}{2})\cos(\frac{\theta}{2}) \end{pmatrix} = |\psi_e\rangle\,.
\end{aligned}
\tag{7}
$$

In this case, the coupling strength g is the dimensionless pulse area, rather than the interaction strength employed in classical experiments. According to the entangled state $|\psi_e\rangle$ of the measured system and the measuring pointer obtained from Eq. (7), we can select an appropriate final state of the measured system for postselection. In this paper, the $|\downarrow\rangle$ is selected as the final state of the measured system. After the postselection operation, the operation that project the measuring pointer onto $|\uparrow\rangle$ and $|\downarrow\rangle$ can be represented as $(\langle\downarrow|\otimes\langle\uparrow|)$ and $(\langle\downarrow|\otimes\langle\downarrow|)$, respectively; these correspond to measure the probabilities of the whole system projecting onto $|3\rangle$ and $|4\rangle$. The final measurement results can be expressed as:

$$
\begin{aligned}
(\langle\downarrow|\otimes\langle\uparrow|)\,|\psi_e\rangle &= \langle 3|\psi_e\rangle = \cos(\frac{g}{2})\sin(\frac{\theta}{2}), \\
(\langle\downarrow|\otimes\langle\downarrow|)\,|\psi_e\rangle &= \langle 4|\psi_e\rangle = -i\sin(\frac{g}{2})\cos(\frac{\theta}{2}).
\end{aligned}
\tag{8}
$$

Here, we can define the finite-coupling postselected pointer ratio (FCPR) [30]:

$$
\langle\hat{\sigma}_x\rangle_{FCPR} = \frac{\langle 4|\psi_e\rangle}{\langle 3|\psi_e\rangle} = \frac{-i\sin(\frac{g}{2})\cos(\frac{\theta}{2})}{\cos(\frac{g}{2})\sin(\frac{\theta}{2})} = -i\tan(\frac{g}{2})\cot(\frac{\theta}{2}).
\tag{9}
$$

Using the traditional weak value $\langle\hat{\sigma}_x\rangle_w = \cot(\frac{\theta}{2})$ defined in Equation (2), the FCPR defined in Equation (9) can be rewritten as $\langle\hat{\sigma}_x\rangle_{FCPR} = -i\tan(\frac{g}{2})\langle\hat{\sigma}_x\rangle_w$. The FCPR can be amplified by choosing the phase angle θ close to the postselection-orthogonal limit, even when the coupling strength g is small; in the weak-coupling limit it reduces to $\langle\hat{\sigma}_x\rangle_{FCPR} \approx -i\frac{g}{2}\langle\hat{\sigma}_x\rangle_w$. In addition, our scheme only requires measuring the probability distribution of the spin state, which significantly reduces the duration of a single weak measurement experiment.

In summary, this scheme enables rapid readout of the postselected pointer response and preserves weak-value-type amplification through single-particle multi-level encoding.

To evaluate how to determine suitable parameters g and θ in this scheme that yield an optimal measurement scheme, we perform the standard Quantum Fisher Information (QFI) approach on the weak measurement scheme described in this paper (see Appendix A for a detailed analysis). According to the definition of QFI $F_Q(g) = 4[\langle\partial_g\psi_e|\partial_g\psi_e\rangle - |\langle\psi_e|\partial_g\psi_e\rangle|^2]$ for a pure state, the QFI of entangled state $|\psi_e\rangle$ is:

$$\begin{aligned} F_Q(g) &= 4 * [\frac{1}{4} - 0] = 1; \\ F_Q(\theta) &= 4 * [\frac{1}{4} - 0] = 1. \end{aligned} \tag{10}$$

Therefore, parameters g and θ in this scheme do not affect QFI. Additionally, based on the Classical Fisher Information (CFI) definition $F_C = \sum \frac{(\partial_g P_i)^2}{P_i}$, we calculate the weak measurement CFI with g as a parameter:

$$F_c^{post}(g) = (\sin\frac{g}{2}\sin\frac{\theta}{2})^2 + (\cos\frac{g}{2}\cos\frac{\theta}{2})^2 + \frac{(\cos\frac{g}{2}\sin\frac{g}{2}\cos\theta)^2}{(\sin\frac{g}{2}\sin\frac{\theta}{2})^2 + (\cos\frac{g}{2}\cos\frac{\theta}{2})^2}. \tag{11}$$

Therefore, based on Eq. (11), we can select suitable experimental parameters so that the experimental CFI approaches the QFI, effectively enhancing the measurement accuracy of the experiment.

3. Experimental setup

This section provides a detailed description of an experimental scheme for performing weak measurements using the multi-level of a single $^{40}Ca^+$ ion in a trapped ion system. A single $^{40}Ca^+$ ion is trapped by a linear Paul trap with an axial trapping frequency $\omega_z \approx 2\pi \times 1.33$ MHz and a radial trapping frequency $\omega_r \approx 2\pi \times 1.6$ MHz. Fig. 1 illustrates the $^{40}Ca^+$ ion energy level diagram and the encoding scheme for the states in the weak measurement scheme. We encode the system states $|1\rangle$, $|2\rangle$, $|3\rangle$, and $|4\rangle$ defined in the previous scheme onto the Zeeman levels $\left|D_{m_J=-3/2}\right\rangle$, $\left|D_{m_J=-1/2}\right\rangle$, $\left|D_{m_J=1/2}\right\rangle$, and $\left|D_{m_J=3/2}\right\rangle$, respectively, of the metastable $\left|D_{5/2}\right\rangle$ level of the $^{40}Ca^+$ ion. The magnetic field $B \approx 11.8$ Gs in the experimental system. To perform rotational operations between the various states of the system, it is necessary to utilize the auxiliary level $\left|S_{m_J=-1/2}\right\rangle$ (defined as $|0\rangle$). A narrow-linewidth 729 nm laser beam can connect the $\left|D_{5/2}\right\rangle$ and $\left|S_{1/2}\right\rangle$ energy levels, with the transition Rabi frequency maintained around $2\pi \times 15$ kHz and the Lamb-Dicke parameter around 0.08. To improve the experimental accuracy, the linewidth of the 729 nm laser beam was locked to within 20 Hz using a PDH frequency stabilization scheme. As the $\left|P_{1/2}\right\rangle$ level has a short lifetime, Doppler cooling and EIT cooling can be achieved by coupling it to the $\left|S_{1/2}\right\rangle$ level via a 397 nm laser beam, thereby improving the fidelity of the operation and the preparation of the initial state. The $\left|P_{1/2}\right\rangle$ can spontaneously transition to the $\left|D_{3/2}\right\rangle$ with a probability; the 866 nm laser beam can repump the ion back to the $\left|P_{1/2}\right\rangle$, thereby ensuring that the cooling cycle proceeds normally. Before performing coherence operations on the ions, the average number of phonons in the motional state of the ion is cooled to below 0.2 . In addition, an 854 nm laser beam can couple the $\left|P_{3/2}\right\rangle$ and $\left|D_{5/2}\right\rangle$ energy levels, thereby enabling quantum state repumping of system.

Since the transition frequency difference between the sublevels of $\left|D_{5/2}\right\rangle$ is 9.91 MHz, it is necessary to utilize the auxiliary energy level $|0\rangle$ to perform rotational operations between system states. Therefore, the operation in Eq. (7) needs to be rewritten; for example, $R_{y_{24}}(\theta)$ must be implemented through $R_{y_{04}}(\pi)\,R_{y_{20}}(\theta)$, where $R_{y_{04}}(\pi)$ represents the application of a π-pulse. Fig. 2 shows the circuit diagram of the rotation operation to

be performed, where the boxes represent the rotation operations to be performed, with the top and bottom of each box corresponding to the system states to be applied. Consequently, the complete experimental sequence can be described as follows: After Doppler cooling and EIT cooling, the single-ion internal state is prepared to $\left|S_{m_J=-1/2}\right\rangle$ ($|0\rangle$) using optical pumping. A π-pulse $R_{y_{01}}(\pi)$ pumps the internal state to $|1\rangle$, following which the rotation operation $R_{y_{03}}(\pi) R_{y_{10}}(\theta)$ prepares the initial state of the system as an arbitrary state with an angle of $\theta = \Omega_{01} t$. Where $\Omega_{01} \approx 2\pi \times 14.8$ kHz is the Rabi frequency for the transition from $|0\rangle$ to $|1\rangle$, and t is the coupling time. The coupling between the measured system and the measuring pointer can be implemented through a set of rotational operations $R_{x_{04}}(\pi) R_{x_{10}}(g) R_{x_{02}}(\pi) R_{x_{30}}(g)$. The coupling strength is set to $g = \Omega_{03} t_{03} = \Omega_{01} t_{01}$, where $\Omega_{03} \approx 2\pi \times 15.7$ kHz is the Rabi frequency between $|0\rangle$ and $|3\rangle$. The entangled state $|\psi_e\rangle$ is prepared. Postselection can be achieved by rotating the measured state to the $|0\rangle$ and then measuring its probability distribution using the electron shelving technique. The $|3\rangle$ corresponds to the probability distribution for the measurement pointer being at $|\uparrow\rangle$, while the $|4\rangle$ corresponds to the probability distribution for the measurement pointer being at $|\downarrow\rangle$.

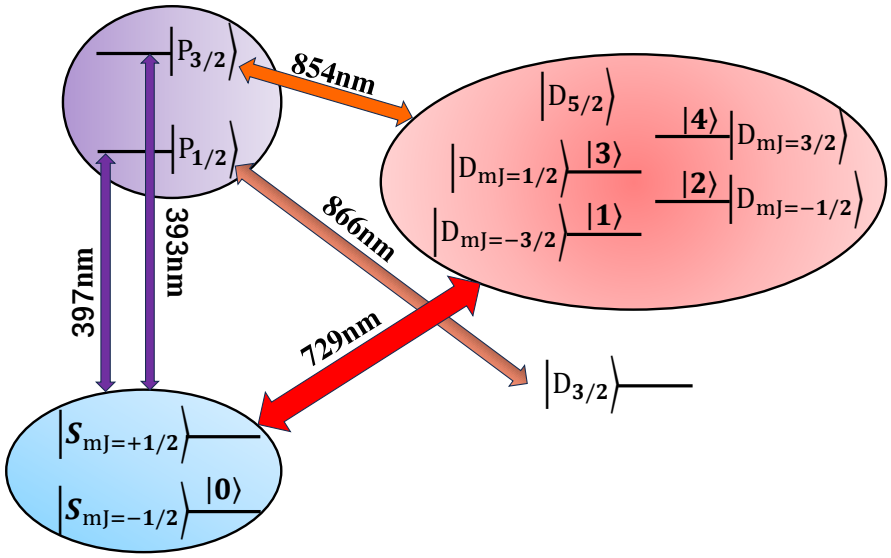


Figure 1: Energy Level Scheme of $^{40}Ca^{+}$ and Encoding Scheme. The quantum state of the system is encoded in the Zeeman sublevels of the $^{40}Ca^{+}$ ion. The ground state $\left|S_{m_J=-1/2}\right\rangle$ is chosen as the auxiliary level $|0\rangle$, while the Zeeman sublevels $\left|D_{m_J=-3/2}\right\rangle$, $\left|D_{m_J=-1/2}\right\rangle$, $\left|D_{m_J=1/2}\right\rangle$, and $\left|D_{m_J=3/2}\right\rangle$ of the metastable state $\left|D_{5/2}\right\rangle$ are selected as $|1\rangle$, $|2\rangle$, $|3\rangle$, and $|4\rangle$, respectively. The rotational operation between the ground state $\left|S_{1/2}\right\rangle$ and the metastable state $\left|D_{5/2}\right\rangle$ can be accomplished using a 729 nm laser beam. The energy level $\left|P_{1/2}\right\rangle$ is connected to the energy level $\left|S_{1/2}\right\rangle$ via a 397 nm laser beam, which can be utilized for laser cooling and quantum projection measurements. The 866 nm laser is used to repump the ion leaking into the $\left|D_{3/2}\right\rangle$ back to the $\left|P_{1/2}\right\rangle$, achieving the cooling cycle. The energy level $\left|P_{3/2}\right\rangle$ is connected to the energy level $\left|D_{5/2}\right\rangle$ via an 854 nm laser beam, accomplishing quantum state repump.

According to the experimental procedure described above, acquiring FCPRs requires only a measurement of the measuring pointer using the electron shelving technique, a process that takes merely $300\mu s$. However, in previous weak measurement experiments using the motion state as a measuring pointer, the data acquisition time for wave packet reconstruction in a single experiment exceeded 4 ms [23–25], and the data also required

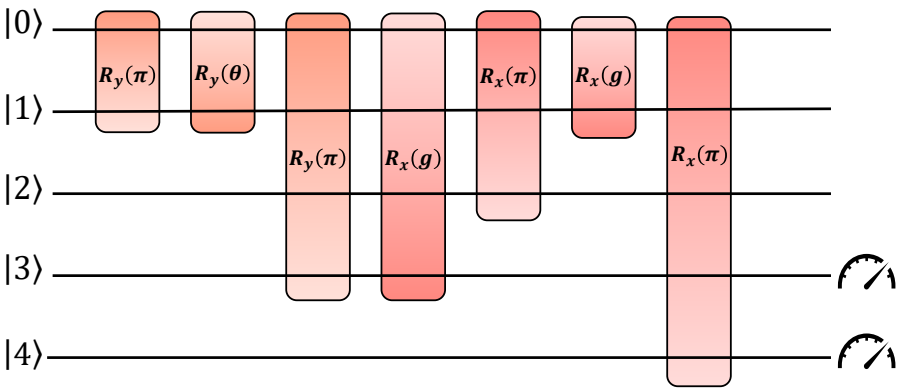


Figure 2: Illustration of a quantum circuit for weak measurement using a single qubit. The system state is encoded in multi-level single-bit states $|1\rangle$, $|2\rangle$, $|3\rangle$ and $|4\rangle$, with level $|0\rangle$ serving as the auxiliary state. The squares represent single-bit rotation gates, with each square indicating the type of rotation gate to be implemented and the corresponding rotation angle. The end of the circuit marks the quantum state to be measured.

additional post-processing. It demonstrates the advantage of our scheme over standard single-particle weak measurement in terms of obtaining measurement results rapidly.

4. Experimental result and discussion

To demonstrate the weak measurement scheme based on single-particle multi-level system, we performed the weak measurement described in the experimental setup above, in which both the measured system and the measuring pointer are the states of a trapped ion qubit. In this paper, experiments are divided into two groups: one group focuses on the fixed coupling strength g between the measured system and the measuring pointer, and the other group focuses on the fixed phase angle θ between the initial and final states of the measured system. According to Eq. (8), with fixed coupling strength $g = \frac{\pi}{2}$, the theoretical results for the probability distributions of the measuring pointer in different final states are $|\langle 3|\psi_e\rangle|^2 = \frac{1}{2}(\sin(\frac{\theta}{2}))^2$ and $|\langle 4|\psi_e\rangle|^2 = \frac{1}{2}(\cos(\frac{\theta}{2}))^2$, respectively. These results are shown in Fig. 3 (a). In addition, Fig. 3 (b) shows the results obtained by scanning the coupling strength g for a phase angle $\theta = \frac{\pi}{2}$ between the initial and final states of the measured system. According to Eq. (8), the theoretical probability distribution of the measuring pointer being in different final states is $|\langle 3|\psi_e\rangle|^2 = \frac{1}{2}(\cos(\frac{g}{2}))^2$ and $|\langle 4|\psi_e\rangle|^2 = \frac{1}{2}(\sin(\frac{g}{2}))^2$. In the experiment, the scanning range for both the phase angle θ and the coupling strength g is from 0 radians to 3π radians, with a scanning step of 0.03π radians. The error bars in Fig. 3 represent the absolute standard uncertainty obtained by calculating the uncertainty of the binomial distribution in the electronic shelving measurement. To minimize the impact of this noise on the

experiment, all experiments were repeated 1,000 times. In addition, frequency drift and power fluctuations in the 729 nm laser beam can also reduce the fidelity of single-qubit rotational operations, thereby affecting the accuracy of the experimental results. This error can be reduced by improving the stability of the laser frequency and power.

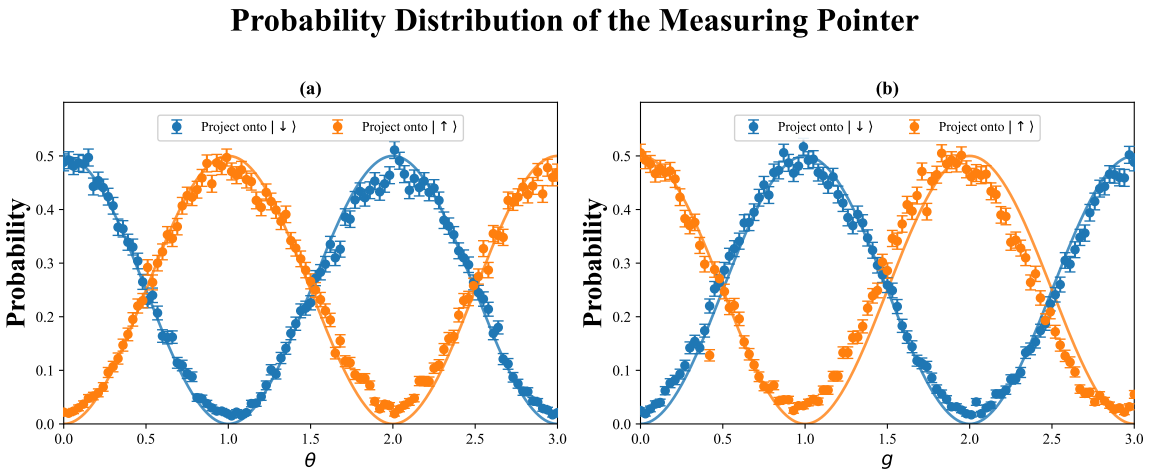


Figure 3: The figure shows the measurement results obtained by projecting the measurement pointer onto different states. In particular, Figure (a) displays the results obtained by varying the phase angle θ between the initial and final states of the measured system while keeping the coupling strength g constant; the horizontal axis represents the phase angle θ in units of π. Figure (b) shows the results obtained by scanning the coupling strength g while keeping the phase angle θ between the initial and final states of the measured system constant; the horizontal axis represents the coupling strength g in units of π. Within the figure, blue dots represent experimental data for the distribution probability when the measuring pointer is projected onto $|\downarrow\rangle$, and red dots represent experimental data for the distribution probability when the measuring pointer is projected onto $|\uparrow\rangle$. The error bars denote the absolute binomial standard uncertainty $\sigma_p = \sqrt{p(1-p)/1000}$ of the measured probabilities. The solid lines represent the theoretical results.

Eq. (9) can be used to calculate the FCPR defined in this paper, as shown in Fig. 4. The theoretical FCPRs of the fixed coupling strength g and the phase angle θ between the initial and final states are $|\langle\hat{\sigma}_x\rangle_{FCPR}| = \cot(\frac{\theta}{2})$ and $|\langle\hat{\sigma}_x\rangle_{FCPR}| = \tan(\frac{g}{2})$, respectively. Experimental data generally matches theoretical values with high accuracy, whilst demonstrating the particular phenomenon that the range of the FCPRs is wider than the native spectrum of the measurement operator. The error bars in Fig. 4 represent the absolute uncertainty derived from the error values of the data shown in Fig. 3 using error propagation formula. According to the error analysis, the region where FCPRs approach extreme values exhibits an approximately 10% error introduced by quantum projection noise, which is the primary source of error. To reduce this type of error, the number of experimental repetitions could be increased. Additionally, a single qubit operation with 99% fidelity will contribute approximately 7.7% error to the experimental results. Furthermore, we evaluated the impact of phase noise originating from the frequency drift of the laser and magnetic field fluctuations. Our simulations indicate that this phase noise contributes a cumulative maximum error of approximately 1.1%. If a step to calibrate the transition frequency is added before each weak measurement experiment, this source of error can be neglected. The weak measurement theory scheme proposed in this paper achieves the interaction between the

measured system and the measuring pointer by decomposing a two-qubit interaction into multiple single-qubit interactions. In practical experiments, due to Rabi frequency fluctuations, the angles of single-qubit rotations may not be well-matched, which can affect the experimental results. We performed a detailed analysis of how this source of error affects the experiment (see Appendix B for details). Suppose the perturbations to the coupling strength g and the initial phase angle θ are Δg and $\Delta\theta$, respectively. The relative error of the FCPR is:

$$\frac{\langle\sigma_x\rangle'_{FCPR} - \langle\sigma_x\rangle_{FCPR}}{\langle\sigma_x\rangle_{FCPR}} \approx \frac{\Delta g}{2}\cot(g) - \frac{\Delta\theta}{\sin(\theta)}. \tag{12}$$

Based on Eq. (12), selecting suitable parameters g and θ in actual experiments can reduce the impact of disturbances on the experiment. Secondly, improving the stability of the Rabi frequency can fundamentally minimize the effect of this error.

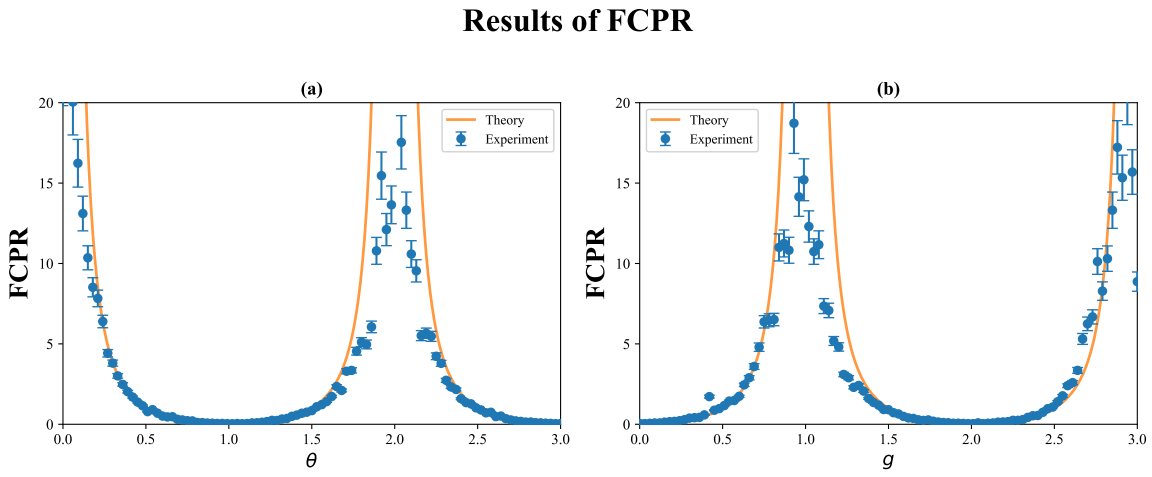


Figure 4: Measurement Results for FCPRs. Figure (a) shows the FCPR of scanning the phase angle between the initial and final states, with fixed coupling strength g. The horizontal axis represents the phase angle between the initial and final states, in units of π, and the vertical axis represents the magnitude of the FCPR. Figure (b) shows the FCPRs of the scanning coupling strength g with a fixed phase angle between the initial and final states. The horizontal axis represents the magnitude of the coupling strength g, in units of π, and the vertical axis represents the magnitude of the FCPRs. The blue dots represent experimental data, and the orange solid line represents the theoretical results. The error bars denote the absolute standard uncertainty σ_{FCPR} of $\langle\hat{\sigma}_x\rangle_{FCPR}$, obtained by propagating the binomial uncertainties of Fig. 3 according to $\sigma_{FCPR} = \frac{|\langle\hat{\sigma}_x\rangle_{FCPR}|}{2}\sqrt{\left(\frac{\sigma_{p3}}{p_3}\right)^2 + \left(\frac{\sigma_{p4}}{p_4}\right)^2}$. The figure shows that a weak-value-type amplification phenomenon occurs near $\theta = 2\pi$ or $g = \pi$, which will be beneficial for precision metrology.

As an example of application of our scheme, we demonstrate laser power monitoring based on our scheme. According to Eq. (9), the magnitude of the FCPR is governed by the coupling strength g and the phase angle θ between the initial and final states. However, in this scheme, both the coupling strength g and the phase angle θ are directly proportional to the magnitude of the Rabi frequency associated with the transition between energy levels $|S_{1/2}\rangle$ and $|D_{5/2}\rangle$ of the trapped ion. Hence, with fixed coupling strength g and phase angle θ, power fluctuations in the 729 nm laser beam will affect the FCPR results. Assuming that the variation in the

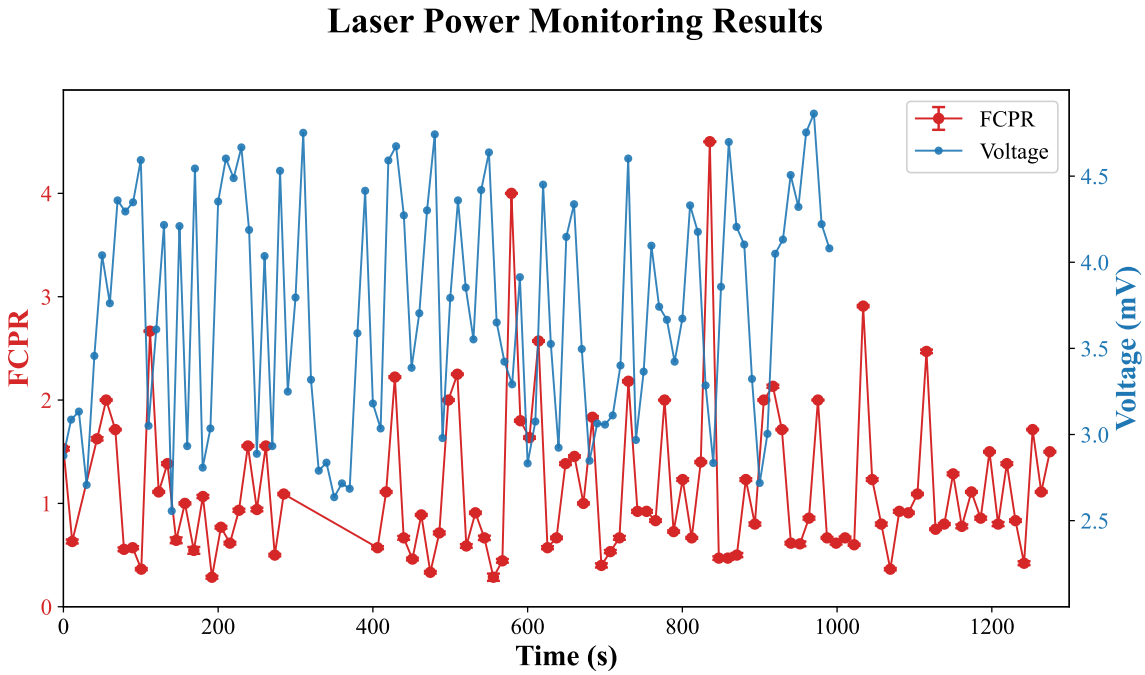


Figure 5: Coherent Control Laser Beam Power Monitoring Results. Red dots represent monitoring results using weak measurement, while blue dots represent monitoring results from photodetector. The horizontal axis represents monitoring duration in seconds. The red vertical axis represents the FCPR, while the blue axis represents the measurement signal from the photodetector (in millivolts).

Rabi frequency caused by laser power fluctuations in a weak measurement experiment is, on average, $\Delta\Omega$, the FCPR can be rewritten as:

$$\begin{aligned} |\langle\hat{\sigma}_x\rangle_{FCPR}| &= \left|\tan(\frac{(\Omega_{03}+\Delta\Omega)t_2}{2})\cot(\frac{(\Omega_{01}+\Delta\Omega)t_1}{2})\right| \\ &= \left|\tan(\frac{g+\Delta\Omega t_2}{2})\cot(\frac{\theta+\Delta\Omega t_1}{2})\right|, \end{aligned} \tag{13}$$

where t_2 and t_1 represent the coupling time and the initial state preparation time, respectively. Based on Eq. (11) and Eq. (12), we set the experimental parameters to $g = \frac{\pi}{2}$ and $\theta = \frac{3}{2}\pi$ to maximize experimental fidelity and CFI; the FCPR of this configuration is theoretically 1. Additionally, at $g = \frac{\pi}{2}$, the first-order contribution of perturbation Δg cancels because $\cot(g) = 0$; this conclusion holds specifically for the symmetric differential-mismatch model adopted in Appendix B, $g_1 = g + \frac{\Delta g}{2}$ and $g_2 = g - \frac{\Delta g}{2}$. Laser power fluctuations induce significant variations in the readout due to the FCPR amplification effect. As shown in Fig. 5, approximately 20 minutes after laser locking, the FCPR (red dots) exhibits substantial residual fluctuations, while simultaneous monitoring of the branch beam with a photodetector (blue dots) reveals no discernible power drift, with the signal dominated by electrical noise. To quantify the difference in response, we compute the coefficient of variation $\delta = \frac{\sigma}{\mu}$ for each channel, where σ is the standard deviation of the data and μ is the mean of the data. The results show that the coefficient of variation of the FCPR (δF) is 0.649, while that of the photodetector signal (δP) is 0.181, giving a normalized fluctuation-response ratio $\frac{\delta F}{\delta P} \approx 3.6$. Because the FCPR and photodetector channels are different observables and have not been independently calibrated against the same laser-power input, this ratio is interpreted as a normalized fluctuation-response ratio rather than a calibrated sensitivity

or signal-to-noise-ratio gain. The comparison indicates that the FCPR readout provides a substantially larger normalized response to residual laser-power fluctuations. The 2.5 mV value is the measured root-mean-square electrical noise floor of the photodetector channel; the larger normalized response of the FCPR readout makes these fluctuations visible above that noise floor, although this observation does not by itself establish a calibrated sensitivity enhancement. This practical response advantage is also consistent with the calculated result $CFI = 0.5 < QFI = 1$: the present scheme trades information-theoretic measurement optimality for single-particle fast readout and enhanced normalized fluctuation response.

5. Conclusion

In summary, we present a new weak measurement scheme where both the measured system and the measuring pointer in standard weak measurement are mapped to the multi-levels of a single particle. This scheme significantly reduces the measurement time required for weak measurement while still achieving standard weak measurement. Consequently, we designed an experiment to monitor fluctuations in laser power, demonstrating the fast measurement advantages and the weak-value amplification effect of the scheme proposed in this paper. Although this paper uses a trapped $^{40}Ca^{+}$ system to experimentally verify the weak measurement scheme, any physical system capable of achieving a coding dimension of 4 or greater can implement this scheme. For example, trapped ion systems exploiting Zeeman or hyperfine sublevels (Yb^{+}, Ca^{+}, Ba^{+}, Sr^{+}); transmon qudits in superconducting circuits; Rydberg atoms and photonic qudits with high-dimensional encoding; and polar molecules with rich rotational level structures.

The present analysis employs standard Quantum Fisher Information theory to evaluate the experimental scheme. It is found that the scheme proposed in this paper is not the optimal scheme in an information-theoretic sense; it merely amplifies the signal to overcome the background noise of the experimental apparatus. Moreover, the scheme presented in this paper also has some challenging limitations: First, this scheme implements interactions through the Hamiltonian in Equation (3); therefore, the coupling strength g can only be applied to a limited set of operators, thereby restricting the scope of the scheme. Second, the sequential operation of multiple single-qubit gates significantly affects the overall experimental fidelity. To improve the overall experimental fidelity, it is necessary to either increase the fidelity of single-qubit operations or optimize the experimental protocol to reduce the number of single-qubit gates. Despite these limitations, this scheme serves as a direct alternative to standard weak measurements, with its ability to rapidly obtain FCPRs offering potential applications in areas such as quantum state tomography, measurements of non-Hermitian operators, and real-time parameter monitoring.

Appendix A: Fisher information analysis

In this section, we calculate the Quantum Fisher Information (QFI) [31] to evaluate the effects of the coupling strength g and the phase angle θ between the initial and final states on the measurement scheme proposed in this paper.

According to the scheme described in this paper, the measured system and the measuring pointer are

coupled to obtain a pure state:

$$|\psi_e\rangle = \begin{pmatrix} \cos(\frac{g}{2})\cos(\frac{\theta}{2}) \\ -i\sin(\frac{g}{2})\sin(\frac{\theta}{2}) \\ \cos(\frac{g}{2})\sin(\frac{\theta}{2}) \\ -i\sin(\frac{g}{2})\cos(\frac{\theta}{2}) \end{pmatrix}. \tag{14}$$

Based on the definition of QFI $F_Q(g) = 4[\langle\partial_g\psi_e|\partial_g\psi_e\rangle - |\langle\psi_e|\partial_g\psi_e\rangle|^2]$, the QFI for parameters g and θ can be calculated as respectively:

$$\begin{aligned} F_Q(g) &= 4 * [\frac{1}{4} - 0] = 1; \\ F_Q(\theta) &= 4 * [\frac{1}{4} - 0] = 1. \end{aligned} \tag{15}$$

This is the ultimate precision bound: any measurement strategy can achieve at most Fisher information F = 1 for estimating the coupling strength g and the phase angle θ from this state. Subsequently, we calculate the Classical Fisher Information (CFI) for the measurement scheme proposed in this paper to evaluate the accuracy of the scheme. If without post-selection, the probability distribution of all states after the measured system is coupled with the measuring pointer:

$$\begin{aligned} P_1 &= |\langle 1|\psi_e\rangle|^2 = (\cos(\frac{g}{2})\cos(\frac{\theta}{2}))^2; \\ P_2 &= |\langle 2|\psi_e\rangle|^2 = (\sin(\frac{g}{2})\sin(\frac{\theta}{2}))^2; \\ P_3 &= |\langle 3|\psi_e\rangle|^2 = (\cos(\frac{g}{2})\sin(\frac{\theta}{2}))^2; \\ P_4 &= |\langle 4|\psi_e\rangle|^2 = (\sin(\frac{g}{2})\cos(\frac{\theta}{2}))^2. \end{aligned} \tag{16}$$

Based on the definition of CFI $F_C = \sum \frac{(\partial_g P_i)^2}{P_i}$, the CFI without post-selection can be calculated as:

$$\begin{aligned} F_C^{full}(g) &= \sum_{i=1}^{4} \frac{(\partial_g P_i)^2}{P_i} = 1; \\ F_C^{full}(\theta) &= \sum_{i=1}^{4} \frac{(\partial_\theta P_i)^2}{P_i} = 1. \end{aligned} \tag{17}$$

Therefore, if the post-selection is not performed, the CFI of this scheme is equal to its QFI, making it the optimal measurement scheme. However, the weak-value amplification effect requires post-selection. Based on the actual experimental setup, we calculated the CFI with post-selection, using the parameter g (coupling strength) as an example. In the weak measurement scheme, only sates $|3\rangle$ and $|4\rangle$ are measured (postselection on $|d\rangle$ for the measured system). This is effectively a 3-outcome measurement: P_3, P_4 and $1 - P_3 - P_4$ (probability of data discard). At this point, the CFI for the scheme is:

$$\begin{aligned} F_c^{post}(g) &= \frac{(\partial_g P_3)^2}{P_3} + \frac{(\partial_g P_4)^2}{P_4} + \frac{((\partial_g(1 - P_3 - P_4))^2}{1 - P_3 - P_4} \\ &= (\sin\frac{g}{2}\sin\frac{\theta}{2})^2 + (\cos\frac{g}{2}\cos\frac{\theta}{2})^2 + \frac{(\cos\frac{g}{2}\sin\frac{g}{2}\cos\theta)^2}{(\sin\frac{g}{2}\sin\frac{\theta}{2})^2 + (\cos\frac{g}{2}\cos\frac{\theta}{2})^2} \end{aligned} \tag{18}$$

We employ a heat map Fig. 6 to illustrate the results of the above equation. The CFI value for the parameters $g = \frac{\pi}{2}$ and $\theta = \frac{3}{2}\pi$ used in the experiments described in this paper is marked with diamond-shaped points in the Fig. 6. Since its CFI is 0.5, which is lower than the QFI corresponding to this scheme, our experiment does not provide the optimal measurement scheme in terms of information theory. As shown in the Fig. 6, the region where the FCPR approaches its extreme value corresponds to the region where the CFI approaches 1 (equal to the QFI).

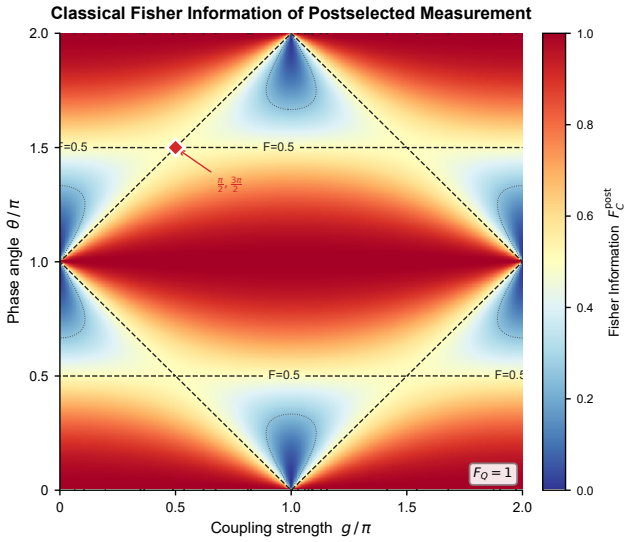


Figure 6: The Classical Fisher Information of PostSelection Measurement. The figure shows the values of the CFI for weak measurements with postselection, as calculated in this paper using coupling strength g as the parameter. The horizontal axis represents coupling strength g, and the vertical axis represents the phase angle θ. The colors range from blue to red, indicating CFI from low to high, with the theoretical maximum equal to 1. The black dashed line represents the contour line for a CFI of 0.5, and the red diamond-shaped points represent the actual experimental parameter settings.

Appendix B: Error Analysis for Pulse Area Mismatch

The core theoretical approach of the weak measurement scheme proposed in this paper is to decompose a two-qubit interaction into multiple single-qubit operations using circuit decomposition. Therefore, according to Equations (5) and (6), both the preparation of the initial state and the coupling process must be decomposed into two rotation operations. However, if the angles of the two rotation operations are mismatched, this will affect the fidelity of the entire experiment. This section specifically analyzes the impact of such mismatches on the experimental results.

If each step in Equation (7) is different—that is, $g_1 \neq g_2$ and $\theta_1 \neq \theta_2$ —then the operations in Equation 7 modify as follows:

$$\begin{aligned} |\psi_e\rangle &= R_{x_{14}}(g_1)\, R_{x_{23}}(g_2)\, R_{y_{13}}(\theta_1)\, R_{y_{24}}(\theta_2)\, |1\rangle \\ &= \begin{pmatrix} \cos(\frac{g_1}{2})\cos(\frac{\theta_1}{2}) \\ -i\sin(\frac{g_2}{2})\sin(\frac{\theta_1}{2}) \\ \cos(\frac{g_2}{2})\sin(\frac{\theta_1}{2}) \\ -i\sin(\frac{g_1}{2})\cos(\frac{\theta_1}{2}) \end{pmatrix}. \end{aligned} \tag{19}$$

Since $R_{y_{24}}(\theta_2)$ does not actually act on the initial state, θ_2 has no effect on the result. From the above equation, the modified FCPR under parameter mismatch is given by:

$$\langle \sigma_x \rangle'_{FCPR} = -i\frac{\sin(\frac{g_1}{2})}{\cos(\frac{g_2}{2})}\cot(\frac{\theta_1}{2}) \tag{20}$$

Define mismatch parameters:

$$g_1 = g + \frac{\Delta g}{2}, g_2 = g - \frac{\Delta g}{2}, \theta_1 = \theta + \Delta\theta \tag{21}$$

where $\Delta g, \Delta\theta \ll 1$ are the relative mismatches. Apply a first-order Taylor approximation to the coupling strength g in Equation (20):

$$\frac{\sin(\frac{g_1}{2})}{\cos(\frac{g_2}{2})} \approx \frac{\sin(\frac{g}{2}) + \frac{\Delta g}{4}\cos(\frac{g}{2})}{\cos(\frac{g}{2}) + \frac{\Delta g}{4}\sin(\frac{g}{2})} = \tan(\frac{g}{2})\frac{1 + \frac{\Delta g}{4}\cot(\frac{g}{2})}{1 + \frac{\Delta g}{4}\tan(\frac{g}{2})} \approx \tan(\frac{g}{2})(1 + \frac{\Delta g}{2}\cot(g)) \tag{22}$$

Additionally, the approximate formulation for the relative error of the phase angle θ in the initial state is as follows:

$$\frac{\cot(\frac{\theta_1}{2})}{\cot(\frac{\theta}{2})} \approx \frac{\cot(\frac{\theta}{2}) - \frac{\Delta\theta}{2}(\csc(\frac{\theta}{2}))^2}{\cot(\frac{\theta}{2})} = 1 - \frac{\Delta\theta}{\sin(\theta)} \tag{23}$$

The relative error of the FCPR is:

$$\frac{\langle\sigma_x\rangle'_{FCPR} - \langle\sigma_x\rangle_{FCPR}}{\langle\sigma_x\rangle_{FCPR}} = (1 + \frac{\Delta g}{2}\cot(g))(1 - \frac{\Delta\theta}{\sin(\theta)}) - 1 \approx \frac{\Delta g}{2}\cot(g) - \frac{\Delta\theta}{\sin(\theta)} \tag{24}$$

Therefore, in Equation (24), an appropriately selected coupling strength g can be employed to reduce the impact of Δg on the experimental fidelity. Fluctuations in the initial state preparation phase angle affect experimental fidelity; this is primarily related to the stability of the Rabi frequency. Additionally, in the extrema region of the FCPR—that is, where θ approaches 0 or 2π—the FCPR is severely affected by $\Delta\theta$. In this experiment, to demonstrate the advantages of the proposed scheme, parameters $g = \frac{\pi}{2}$ and $\theta = \frac{3}{2}\pi$ were selected such that they are virtually unaffected by the perturbation Δg, and the perturbation $\Delta\theta$ has the minimal impact on the experiment.

Acknowledgment

This work was supported by the Quantum Science and Technology-National Science and Technology Major Project (Grant No. 2021ZD0301605), and the National Natural Science Foundation of China (Grants No. 12004430, 12074433, 12174447, 12204543, 12174448).

References

[1] Menglan Xiong, Qiang Yang, Shizhen Chen, and Hailu Luo 2026 *Phys. Rev. A* **113** 033528.

[2] Lijian Zhang, Animesh Datta, and Ian A. Walmsley 2015 *Phys. Rev. Lett* **114** 210801.

[3] Yuichiro Mori, Jaeha Lee and Izumi Tsutsui 2020 *J. Phys. B: At. Mol. Opt. Phys* **53** 015501.

[4] Jeff S. Lundeen and Charles Bamber 2012 *Phys. Rev. Lett* **108** 070402.

[5] Shengshi Pang and Todd A. Brun 2015 *Phys. Rev. Lett* **115** 120401.

[6] Kai Xu (徐凯), Xiao-Min Hu (胡晓敏), Meng-Jun Hu (胡孟军), Ning-Ning Wang (王宁宁), Chao Zhang (张超), Yun-Feng Huang (黄运锋), Bi-Heng Liu (柳必恒), Chuan-Feng Li (李传锋), Guang-Can Guo (郭光灿) and Yong-Sheng Zhang (张永生) 2024 *Chinese Phys. B* **33** 030602.

[7] Wei-Qian Zhao (赵炜骞), Si-Nan Pang (庞斯楠), Zi-Fu Su (苏子富), Tian-Ming Zhao (赵天明), Jin-Dong Wang (王金东) and Ya-Fei Yu (於亚飞) 2026 *Chinese Phys. B* **35** 020301.

[8] Yakir Aharonov, David Z. Albert, and Lev Vaidman 1988 *Phys. Rev. Lett* **60** 1351.

[9] Jeff S. Lundeen, Brandon Sutherland, Aabid Patel, Corey Stewart and Charles Bamber 2011 *Nature* **474** 188.

[10] G. S. Thekkadath, L. Giner, Y. Chalich, M. J. Horton, J. Banker, and J. S. Lundeen 2016 *Phys. Rev. Lett* **117** 120401.

[11] Justin Dressel, Mehul Malik, Filippo M. Miatto, Andrew N. Jordan, and Robert W. Boyd 2014 *Rev. Mod. Phys* **86** 307.

[12] O. Hosten and P. Kwiat 2008 *Science* **319** 787.

[13] Nicolas Brunner and Christoph Simon 2010 *Phys. Rev. Lett* **105** 010405.

[14] N. W. M. Ritchie, J. G. Story, and Randall G. Hulet 1991 *Phys. Rev. Lett* **66** 1107.

[15] A. Danan, D. Farfurnik, S. Bar-Ad, and L. Vaidman 2013 *Phys. Rev. Lett* **111** 240402.

[16] P. Ben Dixon, David J. Starling, Andrew N. Jordan, and John C. Howell 2009 *Phys. Rev. Lett* **102** 173601.

[17] M. Hallaji, A. Feizpour, G. Dmochowski, J. Sinclair, and A. M. Steinberg 2017 *Nature physics* **13** 540.

[18] Wen-Jie Zou, Yu-Huai Li, Shu-Chao Wang, Yuan Cao, Ji-Gang Ren, Juan Yin, Cheng-Zhi Peng, Xiang-Bin Wang, and Jian-Wei Pan 2017 *Phys. Rev. A* **95** 042342.

[19] K. W. Murch, R. Vijay, and I. Siddiqi 2016 *Superconducting Devices in Quantum Optics* 163.

[20] Jonathan T. Monroe, Nicole Yunger Halpern, Taeho Lee, and Kater W. Murch 2021 *Phys. Rev. Lett* **126** 100403.

[21] E. Il' ichev, S. Van der Ploeg, M. Grajcar, and H.-G. Meyer 2009 *Quantum Inf Process* **8** 133.

[22] J. P. Groen, D. Ristè , L. Tornberg, J. Cramer, P. C. de Groot, T. Picot, G. Johansson, and L. DiCarlo 2013 *Phys. Rev. Lett* **111** 090506.

[23] Chun-Wang Wu, Jie Zhang, Yi Xie, Bao-Quan Ou, Ting Chen, Wei Wu, and Ping-Xing Chen 2019 *Phys. Rev. A* **100** 062111.

[24] Yiming Pan, Jie Zhang, Eliahu Cohen, Chun-wang Wu, Ping-Xing Chen and Nir Davidson 2020 *Nature physics* **16** 1206.

[25] Wenbo Su, Manchao Zhang, Chunwang Wu, Yi Xie, Han Hu, Ting Chen, Tianxiang Zhan, Baoquan Ou, Wei Wu, Jie Zhang and Pingxing Chen 2023 *Phys. Rev. A* **108** 042601.

[26] Anders Sø rensen and Klaus Mø lmer 2000 *Phys. Rev. A* **62** 022311.

[27] Rainer Blatt and David Wineland 2008 *Nature* **453** 1008.

[28] S. Wallentowitz and W. Vogel 1995 *Phys. Rev. Lett* **75** 2932.

[29] Yi Li, Qingyuan Mei, Qing-Xuan Jie, Weizhou Cai, Yue Li, Zhiyuan Liu, Zi-Jie Chen, Zihan Xie, Xu Cheng, Xingyu Zhao, Zhenghao Luo, Mengxiang Zhang, Xu-Bo Zou, Chang-Ling Zou, Yiheng Lin, Jiangfeng Du 2025 *https://doi.org/10.48550/arXiv.2504.16746.*

[30] Tamas Geszti 2010 *Phys. Rev. A* **81** 044102.

[31] Yu-Han Yan (严雨涵), Yan-Ping Tan (谭艳萍), Yan-Yan Lu (陆艳艳), Shao-Jie Xiong (熊少杰) and Zhe Sun (孙哲) 2026 *Chinese Phys. B* **35** 010307.